

Article

# Numerical Investigations of the Kinetic Behavior of Adhering Droplets on the Inclined Windshield in Airflows

Fei Dong \*, Xing Xu and Li Xin

School of Automotive and Traffic Engineering, Jiangsu University, Zhenjiang 212013, China; xuxing0609@163.com (X.X.); xinli1126@163.com (L.X.)

\* Correspondence: jsdxdf@ujs.edu.cn

**Abstract:** A theoretical foundation for implementing surface self-cleaning can be provided by analyzing the motion of adhering droplets in airflow. When driving in rainy circumstances, self-cleaning windshield technology can efficiently guarantee driver safety. In this study, the CLSVOF method is employed to simulate a three-dimensional wind tunnel model, enabling an investigation into the dynamics of droplets adhering to a windshield under the influence of airflow. Subsequent analysis mainly focuses on the impacts of wind velocity and droplet size on the motion patterns and morphological characteristics of the droplets. The temporal evolution of the forces acting on the droplets is examined, along with a comparative analysis of the predominant forces driving droplet motion against other forms of resistance. The results demonstrate that the motion patterns of the droplets can be broadly categorized into three phases: accelerated decline, forces equilibrium, and accelerated climb. As wind speed increases, there is a noticeable reduction in the wetting length  $L_d$ , while the height of the droplets  $H$  and the dominant force influencing their motion shift from gravitational component  $F_g \sin \alpha$  to wind traction force  $F_{wind}$ . Moreover, an increase in droplet size accentuates the lag in changes to wetting length, droplet height, and the contact angle.

**Keywords:** adhering droplet; airflow; windshields; kinetic behavior; force analysis



**Citation:** Dong, F.; Xu, X.; Xin, L. Numerical Investigations of the Kinetic Behavior of Adhering Droplets on the Inclined Windshield in Airflows. *Appl. Sci.* **2024**, *14*, 3763. <https://doi.org/10.3390/app14093763>

Academic Editor: Jianzhong Lin

Received: 5 March 2024

Revised: 23 April 2024

Accepted: 25 April 2024

Published: 28 April 2024



**Copyright:** © 2024 by the authors. Licensee MDPI, Basel, Switzerland. This article is an open access article distributed under the terms and conditions of the Creative Commons Attribution (CC BY) license (<https://creativecommons.org/licenses/by/4.0/>).

## 1. Introduction

The interaction between droplets and solid surfaces is a phenomenon extensively observed in the field of surface self-cleaning [1–4], aimed at reducing or eliminating the adhesion of external fluid contaminants. The removal of droplets through airflow is a crucial aspect of surface self-cleaning research. This method applies the additional force created by airflow to initiate the movement of adherent droplets on surfaces such as machinery and casings, thus achieving the objective of cleaning. In practical engineering applications, variations in airflow environments, droplet properties, and surface wettability can lead to different adhesive behaviors during the interaction process between droplets and solid surfaces [5,6]. An in-depth exploration and application of this technology not only facilitates efficient surface cleaning but also diminishes the dependency on chemical cleaners, consequently reducing environmental pollution and cleaning expenses.

In recent years, surface self-cleaning research has been increasingly harnessed to address rainwater contamination on front windshields. During rainfall, droplets adhere to the windshield surface under the combined influence of their own gravity and the airflow around the window, worsening the driver's visual impairment. A blurred windshield view can distract the driver, leading to visual fatigue and significantly compromising driving safety. Consequently, reducing droplet adhesion on the windshield and promoting droplet movement are critical for alleviating water contamination on the windshield.

Initial approaches to the issue of windshield water contamination brought on by rain concentrated on the continuous optimization of vehicle components to reduce the problem of visual obstruction, including the structure of the wipers [7,8], control strategies [9,10],

and the wetting characteristics of the windshield [11–13]. These techniques can somewhat lessen the amount of precipitation that accumulates on the windshield but cannot reduce the frequency of raindrop impact. Modified windshield coatings are also costly and have a poor response time. These solutions do not address the issue via the investigation of microscopic droplet movement phenomena and causes.

At present, theoretical research on the self-cleaning of droplets on front windshields from the fluid dynamics perspective is an emerging technological field that demands deeper investigations. Understanding the interaction mechanism between droplets and the windshield surface will lay a theoretical foundation for further optimizing the windshield and related components, achieving self-cleaning on the surface, and enhancing driving safety.

The movement of droplets on the windshield in air conditions can be fundamentally reduced to the motion of adherent droplets on the inclined surface under the airflow. A foundational requirement for exploring the theory of self-cleaning on windshields is the extensive investigation of droplet motion in airflow. However, existing studies primarily concentrate on the detachment of adherent droplets on flat surfaces and the investigation of critical air velocity laws, without examining the full motion process of droplets on inclined surfaces. Milne and Amirfazli [14] investigated the shedding behavior of droplets on surfaces with different wettability in shear flow. They concluded that the wetting parameters of droplets on surfaces have important influences on droplet shedding. Roisman et al. [15] proposed a critical air velocity model applicable to droplet height by measuring the critical air velocity for different droplet volumes on substrates with different wettability with the same thickness of the viscous boundary in the airflow. Barwari et al. [16] determined three states of adhering droplets in shear flow just before and after motion. They eventually established their global empirical law by redefining critical air velocity. Hooshanginejad and Lee [17] investigated the interaction of a pair of string droplets in an airflow by experimental and numerical simulations and found that the critical distance for independent shedding of upstream droplets is 2.4 times the baseline length. Razzaghi and Amirfazli [18] investigated critical air velocity versus droplet spacing for droplets moving in an air stream with different alignment patterns, which showed that surface wettability does not affect the overall trend of critical air velocity with droplet spacing. Rohde et al. [19] investigated the effect of vibration on the critical air velocity of droplets by superimposing vibration on a horizontal surface. The results show that the critical air velocity is significantly reduced by superimposed harmonic oscillation. The decrease is particularly noticeable at surface vibration in the range of the first and third eigenfrequency of the droplet. Yeganehdoust et al. [20] explored droplet shedding behavior under different droplet sizes, spacings and airflow velocities through experiments and numerical simulations. A dynamic contact angle model was used to simulate droplet shedding on various wettability surfaces. The changes in drag and lift forces before and after droplet coalescence were also analyzed in detail to better explain the dynamic behavior of droplets. Shi et al. [21] focused on the differences in the behavior of droplets of different volumes on hydrophilic and superhydrophobic surfaces under airflow. It was found that larger droplets on hydrophilic surfaces exhibited longer wetting lengths and stronger adhesion, and that the air velocity was the main reason affecting the sliding and rolling behavior of droplets on superhydrophobic surfaces.

Only a few studies have explored the motion of droplets adhered to inclined surfaces in airflow, primarily concentrating on the forces exerted on droplets. Hashimoto et al. [22] investigated the acceleration of droplets moving in uniform airflows on the windshield by building a wind tunnel. They found that droplets can be classified as sliding, stationary, and climbing at different airflow velocities. Nakata et al. [23] simulated the behavior of droplets on a hydrophobic windshield under driving conditions and proposed a force equation for droplets during the movement. Chen et al. [24] proposed a new method to simulate the water flow of droplets on a tilted glass pane at the moment of rainfall and proved the reliability of the simulation compared with the experimental results. Koblik [25] used a graphical processing method to simulate the behavior of droplets on a tilted windshield

under different combinations of wind and gravity. Correlation between the wind force magnitude and droplet motion was obtained. Edward et al. [26] proposed a mathematical model for the detachment of droplets on inclined surfaces under high-speed airflow, employing direct formulas for surface tension, gravity, and aerodynamic forces. This model plays a crucial role in predicting the critical air velocity. Hu et al. [27] investigated the droplet shedding behavior on metal fiber surfaces with different surface wettability and tilting angles and established predictive correlations for critical droplet sizes on metal fibers with different wettability and different tilting angles, which agreed with the experimental results. Yurishchev et al. [28] considered factors like droplet shape and airspeed in their research into droplet motion on inclined surfaces under airflow. They developed a predictive model for the air resistance coefficient that adapts to changes in influencing factors, making it useful for calculating critical air velocity.

In conclusion, current studies on the detachment behavior of droplets adhering to flat and inclined surfaces in airflow, as well as the forces acting on droplets in an airflow environment, have made significant progress. However, these studies primarily focus on predicting the numerical values of critical air velocity. The forces acting on droplets and their shape changes when they start moving have not been explored. In this study, the coupled CLSVOF method, integrating Volume of Fluid (VOF) and Level-set method, is used for numerical simulation. A three-dimensional wind tunnel model has been developed, and a dynamic contact angle model is employed to accurately simulate the changes in droplets. By considering airflow velocity and droplet size as research variables, the study offers a comprehensive analysis of how these variables influence the motion patterns and shape transformation rules of droplets adhering to inclined windshields. Finally, forces acting on the droplet are calculated. The changes in droplet forces with time are discussed, and the relationship between the dominant force of droplet movement and other resistances is compared.

## 2. Materials and Methods

### 2.1. Numerical Calculation Model

Airflow under natural conditions needs to be simulated, but the computational cost of full-scale wind tunnel numerical simulation is relatively high. Therefore, the scaled-down wind tunnel is usually used to reproduce the outflow field [29]. In order to study the motion of droplets on the windshield at a certain wind speed, the 3D geometric model used for the study is a scaled down model of the inclined surface with model dimensional parameters, as shown in Figure 1.

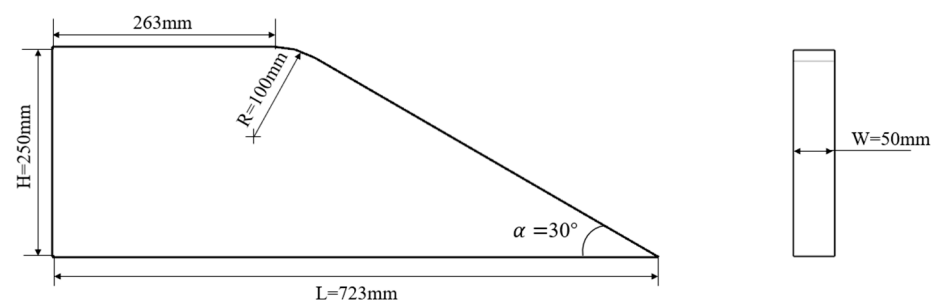


**Figure 1.** Schematic of the 3D model.

According to the wind tunnel design theory, the size of the computational domain used in the numerical simulation needs to be determined based on the size of the three-dimensional model to ensure the accuracy of the computational results, as well as the appropriateness of the computational cost at the mean time. The computational domain and the boundaries used in this study are shown in Figure 2, in which the length is 11 L, the width is 7 W, and the height is 5 H, and L, W, and H are the length, width, and height of the three-dimensional model, respectively. The 3D model is located on the symmetry plane of

the computational domain, and the distance between the trailing edge of the model and the airflow outlet boundary is  $7L$ . In addition, the boundary conditions of the computational domain are shown in Table 1.

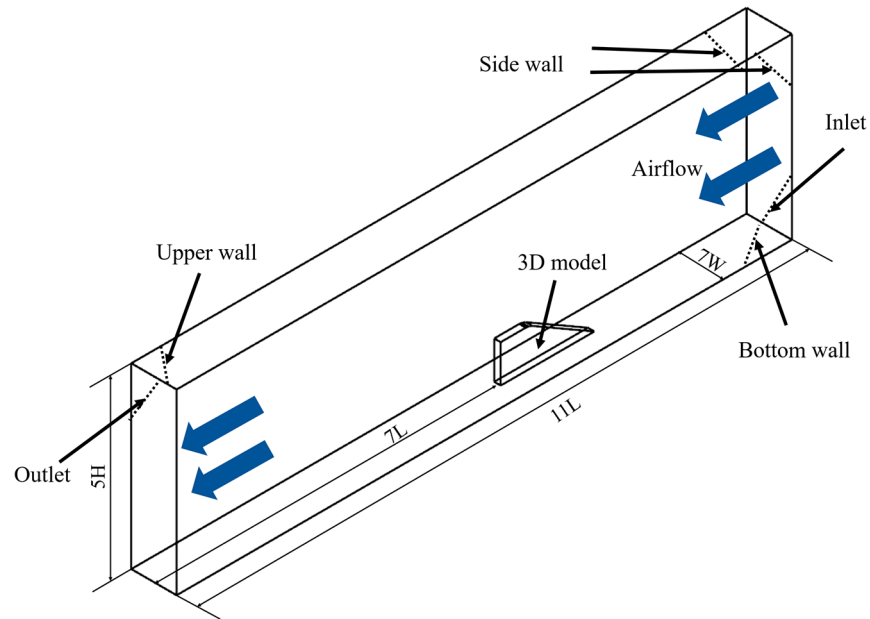


**Figure 2.** Schematic diagram of the computational domain.

**Table 1.** Boundary conditions of the computational domain.

Boundary	Boundary Condition Setting
Inlet of the computational domain	Velocity inlet
Outlet of the computational domain	Pressure outlet
Upper wall and the side wall	Symmetric boundary
3D model and the bottom wall	No slip

Water and air are made as the dispersed phase and continuous phase, respectively. The densities of water and air are  $998.2 \text{ kg/m}^3$  and  $1.225 \text{ kg/m}^3$ , respectively, in the numerical simulation. The viscosities of water and air are  $1.003 \times 10^{-3} \text{ kg/m}\cdot\text{s}$  and  $1.79 \times 10^{-5} \text{ kg/m}\cdot\text{s}$ , respectively. The interfacial tension  $\sigma$  between the droplet and the air is  $0.0728 \text{ N/m}$ .

The droplet adhering to the hydrophilic surface of a windshield in a stationary state is shown in Figure 3a. In actual situations, the droplets appear cap-shaped on the surface. Considering the impact of droplet size on simulation results in numerical simulations, this study investigates droplets with volumes  $V'$  of  $14.14 \text{ }\mu\text{L}$ ,  $22.45 \text{ }\mu\text{L}$ , and  $33.51 \text{ }\mu\text{L}$ , respectively.

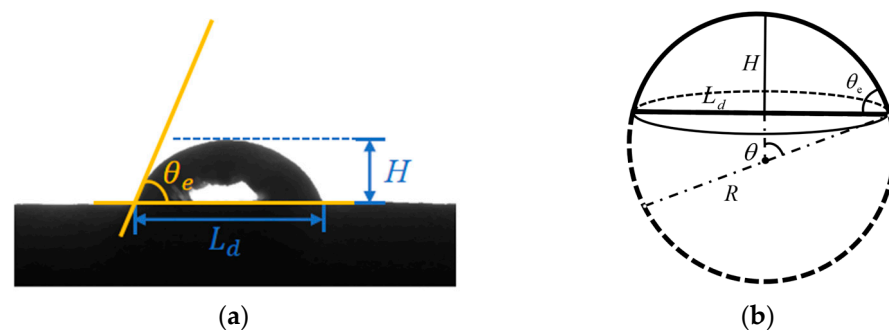


**Figure 3.** Schematic diagrams of the adhesive droplet: (a) Experiment; (b) Numerical stimulation.

Using the spherical volume formula of  $V' = \frac{4\pi}{3} \left(\frac{D}{2}\right)^3$ , the spherical diameters  $D$  of the droplets are determined to be 3 mm, 3.5 mm, and 4 mm, respectively. Future measurements of droplet size will be uniformly annotated based on the spherical diameter  $D$ . To assess the wettability of droplets on the hydrophilic windshield surface, the static contact angle  $\theta_e$  of the droplets was measured. On the substrate of the hydrophilic windshield used, the water droplets studied form a moderate static contact angle  $\theta_e = 66.8^\circ$ .

As shown in Figure 3b, to determine the initial state of droplet motion on the windshield, the initial shape of the droplet on the hydrophilic windshield is considered to be a spherical cap. Based on the droplet volume  $V'$  and the static contact angle  $\theta_e$  on the windshield, the relationship between the spherical radius  $R$ , the wetting length  $L_d$ , and the droplet height  $H$  in the numerical simulation was derived as [30]:

$$R = \left[ \frac{V'}{\frac{\pi}{3}(2 - 3\cos\theta_e + \cos^3\theta_e)} \right]^{\frac{1}{3}} \quad (1)$$

$$L_d = 2R\sin\theta_e \quad (2)$$

$$H = R(1 - \cos\theta_e) \quad (3)$$

Understanding the impact of airflow on droplet motion is crucial to address the issue of morphological alterations of adhering droplets moving on the windshield in the presence of natural airflow. The droplet Weber number ( $We$ ) is introduced to represent the ratio of inertial force to surface tension, which is defined as:

$$We = \frac{\rho_g U^2 D}{\sigma} \quad (4)$$

where  $\rho_g$  is the air density,  $U$  is the air velocity,  $D$  is the spherical diameter of the droplet in the numerical simulation, and  $\sigma$  is the interfacial tension between the droplet and the air.

The size of the Weber number also affects the extent of droplet fragmentation in high-speed gas streams. It needs to be limited to 10 to prevent droplet fragmentation [31]. Therefore, the wind speed  $U$  is set at 3–12 m/s based on numerical calculations.

## 2.2. Numerical Stimulation Methods

In numerical simulations, the Volume of Fluid (VOF) method is commonly utilized to define the interface between gas and liquid phases within a grid. In the VOF method, the  $F$  function is often used to represent the phase function, and the volume fraction  $\beta$  of the lattice liquid occupying the lattice space is calculated by solving the phase function. The phase function is used to characterize the distribution of the gas–liquid phases in the flow field. The definition of the  $F$ -function is shown in Equation (5):

$$F(\vec{r}, t) = \begin{cases} 1, & \text{in the liquid region} \\ 0 < F < 1, & \text{at the interface} \\ 0, & \text{in the gas region} \end{cases} \quad (5)$$

where  $\vec{r}$  is any point in the computational domain and  $t$  is time.

As water in numerical simulations is treated as an incompressible fluid, the primary governing equation for the VOF method is the continuity equation for incompressible fluids, ensuring effective conservation of physical quantities. The mass conservation equation for the  $F$  function can be expressed as:

$$\frac{\partial F}{\partial t} + (\vec{u} \cdot \nabla) F = 0 \quad (6)$$

where  $\vec{u}$  is the velocity of the grid.

Although the VOF method can represent the structure of a complex two-phase interface and its variations with relatively simple calculations, the discontinuity of the function at the phase interface can lead to difficulties in accurately calculating the normal direction of the phase interface, the curvature, and the physical quantities related to the curvature.

The Level-set method defines the evolution equation for the position of the two-phase interface over time. Unlike the VOF method, the Level-set method uses the level set function  $\varphi(\vec{r}, t)$ , expressed as the phase function, to distinguish between different phases in the computational domain. In gas–liquid two-phase flow calculations, the level set function  $\varphi(\vec{r}, t)$  is defined as:

$$\varphi(\vec{r}, t) = \begin{cases} > 0, & \text{in the liquid region} \\ 0 < F < 1, & \text{at the interface} \\ < 0, & \text{in the gas region} \end{cases} \quad (7)$$

The surrogate value of the level set function  $\varphi(\vec{r}, t)$  represents the minimum value of the line connecting the center of the calculation grid and the phase interface. At any time, only the magnitude and direction of the level set function are required to determine the location of the two-phase interface and the distribution of the gas–liquid phase. Therefore, the Level set method can avoid the tedious process of indirectly tracing the phase interface and can improve the ability of tracing the two-phase interface.

In the Level-set method, the equivalence surface of the level set function  $\varphi(\vec{r}, t) = 0$  is the interface and will satisfy the following equation:

$$\frac{D\varphi}{Dt} = \frac{\partial\varphi}{\partial t} + (\vec{u} \cdot \nabla)\varphi = 0 \quad (8)$$

Equation (8) is the convective transport equation for the level set function  $\varphi(\vec{r}, t)$ . Since the function  $\varphi(\vec{r}, t)$  is continuous, Equation (9) can be further rewritten as:

$$\frac{\partial\varphi}{\partial t} + \vec{u}(\nabla \cdot \varphi) = 0 \quad (9)$$

Since the level set function  $\varphi(\vec{r}, t)$  is a distance function, the characteristics of the distance function must also be maintained when performing the calculation. Otherwise, it will result in the loss of fluid mass within the closed phase interface, and the physical quantity is not conserved [32,33]. The function  $\varphi(\vec{r}, t)$  is a continuous function, which facilitates the calculation of parameters, such as the curvature of the phase interface, normal vector, and surface tension. However, the problem of the loss of fluid mass within the interface generated during the function calculation is the biggest defect of this method and one of the difficulties to be solved.

From the introduction of the VOF method and the Level-set method, it can be seen that the VOF method can maintain the conservation of physical quantities and the calculation is relatively simple, but the disadvantage is that its difficulty to accurately solve the interface normal vector, curvature, and other internal geometrical parameters. The Level-set method represents the two-phase interface as a function with  $\varphi(\vec{r}, t) = 0$ , which makes it easier to calculate the parameters, such as curvature, normal vector, and surface tension. The disadvantage of the Level-set method lies in the loss of the fluid mass inside the interface in the process of calculating the function  $\varphi(\vec{r}, t)$ , which does not conserve the physical quantities.

However, the advantages and disadvantages of the VOF method and the Level Set method can complement each other, so the Coupled Level-set method and Volume of Fluid

(CLSVOF) method proposed by Yokoi [34] are used to establish the numerical modelling framework according to the characteristics of both the VOF and Level-set method. The CLSVOF method is based on the VOF model and is modified by introducing the level set function  $\varphi(\vec{r}, t)$ . The CLSVOF method can be applied to the dynamic interface of liquid droplet flow problems, such as wetting, which is related to the attachment of droplets on inclined surfaces with interfacial motion. Firstly, the method will solve the continuity equation and the Navier–Stokes equations in the computational domain [35,36]:

$$\nabla \cdot \vec{v} = 0 \tag{10}$$

$$\frac{\partial}{\partial t} [\rho(\varphi) \vec{v}] + \nabla \cdot [\rho(\varphi) \vec{v} \vec{v}] = -\nabla p + \nabla \cdot \left[ \mu(\varphi) \left( \nabla \vec{v} + \nabla \vec{v}^T \right) \right] + \rho(\varphi) \vec{g} - \vec{F} \tag{11}$$

where  $\vec{v}$  is the velocity vector,  $\vec{g}$  is the gravity, and  $p$  is the pressure.  $\mu(\varphi)$  and  $\rho(\varphi)$  are the dynamic viscosity and density of the droplet, respectively.  $\varphi$  is a function of the level set:

$$\varphi(\vec{r}, t) = \begin{cases} -d, & \text{in the gas region} \\ 0, & \text{at the interface} \\ d, & \text{in the liquid region} \end{cases} \tag{12}$$

where  $d$  is the shortest distance between the interface and the point  $\vec{r}$ .

The inclusion of the level set function  $\varphi(\vec{r}, t)$  allows the calculation of both interface curvature and physical properties to be based on the distance function. The continuity of the level set functions makes the calculation results more accurate. In addition to this, the CLSVOF method will use the method proposed by Brackbill [37] via the CSF (continuous surface force) model, which is the source term of the surface tension imposed by the phase interaction condition solved. This can be expressed smoothly according to the Heaviside function:

$$\vec{F} = \sigma \kappa(\varphi) \nabla H(\varphi) \tag{13}$$

$$H(\varphi) = \begin{cases} 0 & \varphi < -a \\ \frac{1}{2} + \frac{\varphi}{2a} + \frac{1}{2\pi} \sin\left(\frac{\pi\varphi}{a}\right) & |\varphi| \leq a \\ 1 & \varphi > a \end{cases} \tag{14}$$

where  $\kappa(\varphi)$  is the curvature of the liquid surface and  $\sigma$  is the surface tension coefficient.  $H(\varphi)$  is the Heaviside function, which can be used to calculate the physical properties of fluids within the interface.  $a$  is the thickness of the transition zone at the phase interface. The physical properties of fluids  $\rho(\varphi)$  and  $\mu(\varphi)$  can be expressed as:

$$\rho(\varphi) = \rho_g + (\rho_l - \rho_g)H(\varphi) \tag{15}$$

$$\mu(\varphi) = \mu_g + (\mu_l - \mu_g)H(\varphi) \tag{16}$$

where the subscripts  $g$  and  $l$  denote the gas phase and liquid phase, respectively.

To consider the effect of the contact angle via the wall boundary condition, the surface normal at the cell next to the wall is expressed as:

$$\hat{n} = \hat{n}_w \cos\theta + \hat{\tau}_w \sin\theta \tag{17}$$

where  $\hat{n}_w$  and  $\hat{\tau}_w$  are the unit vectors perpendicular and tangent to the wall.

Establishing a steady-state flow field with constant wind speed in the absence of droplets is important to ensure the observation of droplet motion in the presence of a stable external flow field. The droplet motion process on the windshield was then simulated by establishing transient conditions based on the steady-state flow field. Combining the values of the VOF and Level Set functions with the geometric PLIC method, an initialization

procedure is applied after each time step [38]. The calculations are performed on a fixed Eulerian structured grid using the CLSVOF method to follow the gas–liquid interface.

The Mach number of the external flow field of the windshield in the realistic environment is relatively low, and the airflow separation is easily formed around the vehicle during the driving process. Therefore, it can be regarded as an incompressible viscous isothermal flow field. The turbulence model is usually used in the numerical simulation of the external flow field of the car. In this study, the standard  $k-\epsilon$  model is used with good convergence and lower residual values.

The movement of droplets on the windshield surface is influenced by the droplets' physical properties and the surface wettability. The wettability is determined by interactions at the solid–gas, solid–liquid, and gas–liquid interfaces and is assessed using two parameters: the static contact angle  $\theta_e$  and the dynamic contact angle  $\theta_D$ . In the airflow, imbalances in the forces acting on the droplet can lead to dynamic changes in wettability behavior. When the contact line velocity  $U_{cl}$  exceeds 0, the dynamic contact angle is utilized to evaluate the motion of the droplet's contact lines.

When the contact lines begin to move, its dynamic contact angle parameters are illustrated in Figure 4. The contact angle at the onset of wetting by the three-phase contact line is defined as the advancing contact angle  $\theta_{adv}$ , while the contact angle during the retreat of the three-phase contact line along the wetted surface is defined as the receding contact angle  $\theta_{rec}$  [39].

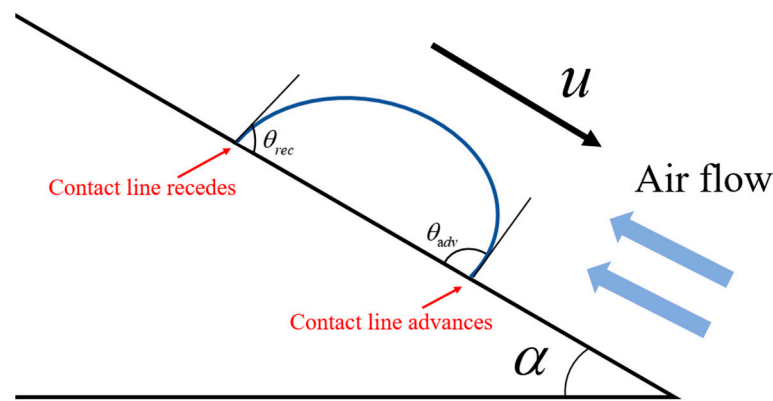


Figure 4. Schematic diagram of the dynamic contact angle parameters.

The dynamic contact angle model used in association with a flow model has been found to be an accurate method to represent the contact angle variation in fluid flow [40]. Thus, the dynamic contact angle is introduced to reproduce the transient contact angle values between the droplet and the wall more accurately. The dynamic contact angle ( $\theta_D$ ) is defined as a function of the contact line velocity in the combination of Kistler and Tanner's methods, which is expanded in the form of the capillary number  $Ca$ , the contact line's diffusion velocity  $U_{cl}$ , the static advancing contact angle  $\theta_{adv}$ , the static receding contact angle  $\theta_{rec}$ , and the Hoffman empirical function  $f_H(x)$  and its inverse  $f_H^{-1}(x)$ . It can be expressed as:

$$\theta_D = \begin{cases} f_H(Ca + f_H^{-1}(\theta_{adv})) & U_{cl} \geq 0 \\ (\theta_{rec}^3 - 72Ca)^{\frac{1}{3}} & U_{cl} < 0 \end{cases} \quad (18)$$

$$f_H(x) = \arccos\left(1 - 2 \tanh\left(5.16 \left(\frac{x}{1 + 1.31x^{0.99}}\right)^{0.706}\right)\right) \quad (19)$$

where the capillary number  $Ca$  is defined as  $Ca = \frac{\mu_l U_{cl}}{\sigma}$ .  $\mu_l$  and  $\sigma$  in the definition equation are the dynamic viscosity and surface tension of the liquid, respectively.

### 2.3. Grid Strategy and Grid Independence Verification

In the numerical simulation of droplet motion in the airflow, the surface mesh fitness will directly affect the accuracy of droplet simulation. Therefore, the mesh of the tilted surface of the windshield and the droplet motion region has high requirements. Thus, a polyhedral mesh is used for spatial discretization of the whole computational domain, and a smooth transition scheme is adopted between different mesh sizes. In this study, the development of the flow field in the inclined area of the 3D model is considered, and the main encrypted area is the inclined area of the model. A total of eight encrypted areas are established in the whole computational domain to ensure the grid size of the inclined area meets the needs of analyzing the droplet motion. In addition, to accurately obtain the flow inside the boundary layer and to satisfy the principle that the  $Y^+$  value is established in the logarithmic law layer, a fine prismatic layer mesh is used to delineate the surface of the window, with the first layer mesh set at 0.1 mm and the growth ratio at 1.1, totaling five layers. The encrypted region and boundary layer division of the whole computational domain are shown in Figure 5.

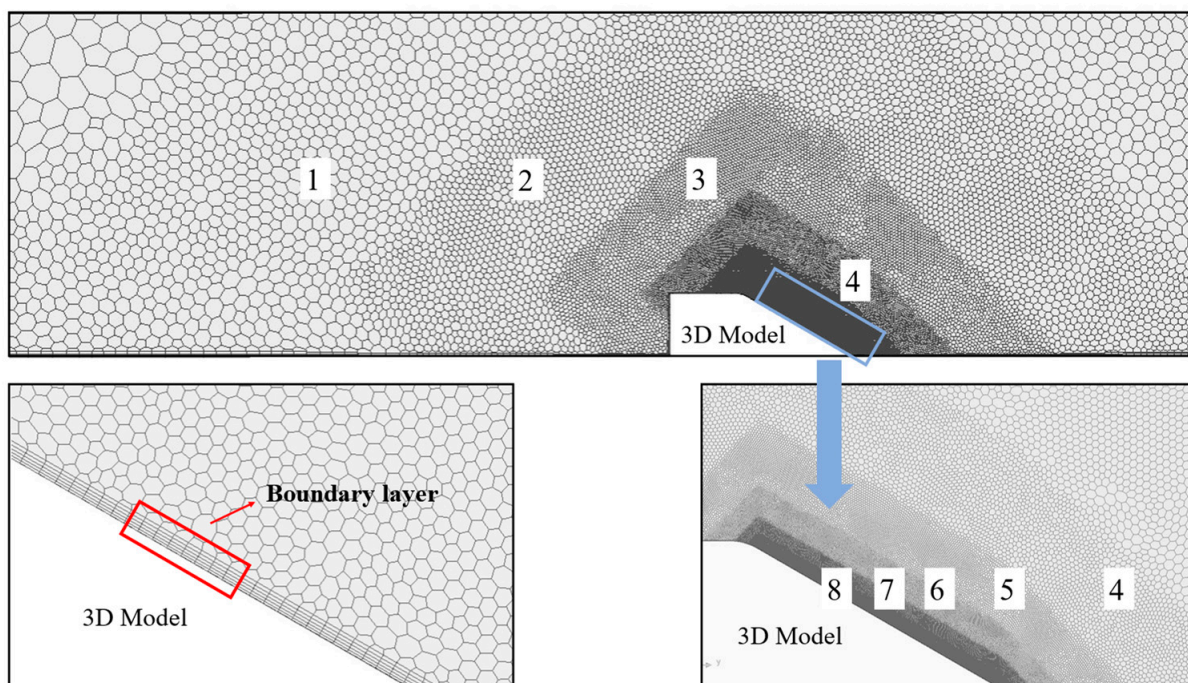


**Figure 5.** Schematic diagram of the numerical model of liquid droplets.

A test of grid independence is required before the numerical simulation calculation. When using the CLSVOF method for the droplet simulation, the minimum mesh size for displaying the droplet morphology needs to be considered. In the grid independence test, the minimum grid size is set to 0.05 mm, 0.1 mm, 0.15 mm, and 0.2 mm. The total number of grids drawn with the same grid strategy are 3,663,255, 2,388,324, 1,446,903, and 1,023,322, respectively. We take a 3 mm diameter droplet with an initial velocity of 0.5 m/s impinging on the inclined plane as an example and compare the droplet spreading factor (the ratio of droplet spreading length to droplet diameter). The comparison results are shown in Figure 6. The results show that a reasonable grid scale is a prerequisite for capturing the phase interface accurately. According to the graphical results, the model with the minimum grid size set to 0.1 mm, which corresponds to the total grid number of 2,388,324, is selected.

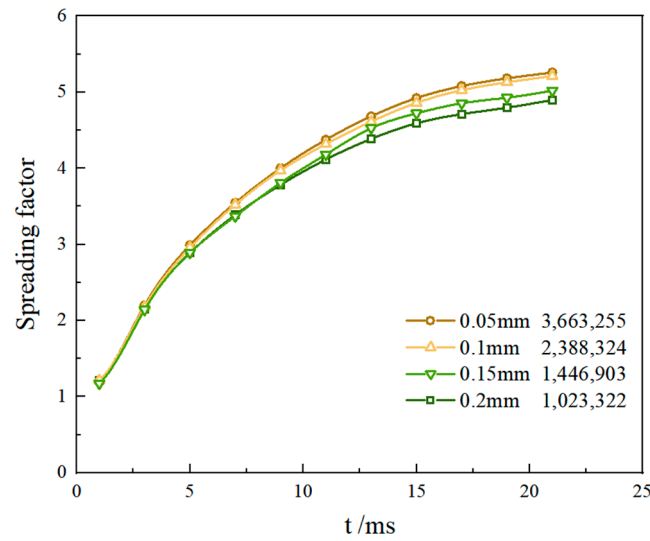


Figure 6. Results of droplet spreading factors under different minimum grid sizes.

### 3. Results and Discussion

#### 3.1. Experiment and Model Validation

During the study, we developed an experimental setup to capture the movement of adhesive droplets on a tilted surface within airflow environment, as illustrated in Figure 7. A high-speed video camera equipped with an image processing system was utilized to record the details of droplet motion under the airflow, while an LED light source provided illumination for the experiments. Airflow was generated using a centrifugal fan, with the wind speed regulated by a wind speed adjustment device. The air passed through a 100 cm long rectifier equipped with damping screens to ensure the stable airflow. The hydrophilic glass substrate had a tilt angle of 30 degrees, identical to tilt  $\alpha$  in the 3D model.

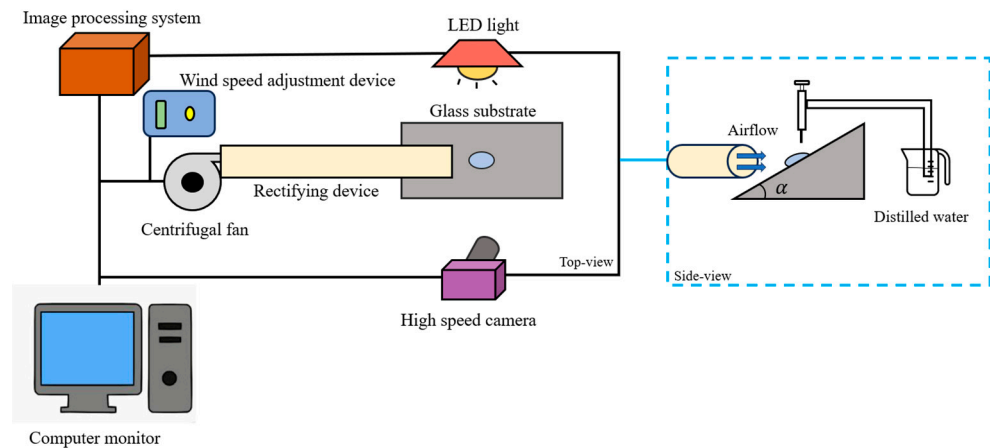
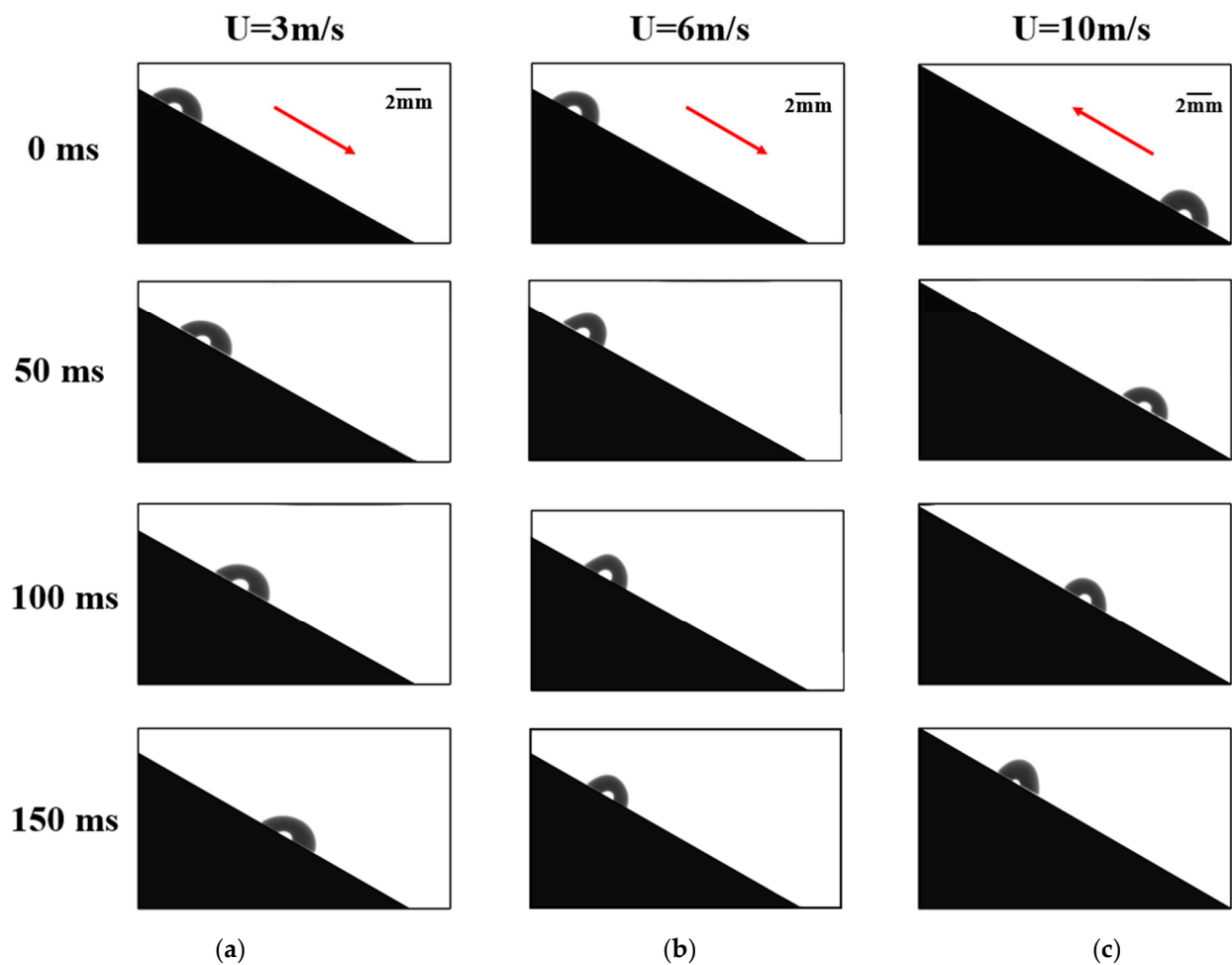


Figure 7. Schematic diagram of the experimental setup.

To ensure the accuracy and reliability of the experimental data, we conducted at least three replicated experiments for each airflow velocity to assess the behavior of the droplets and minimize experimental error. Figure 8 illustrates the dynamic behavior of droplets in airflow environments with velocities of  $U = 3 \text{ m/s}$ ,  $6 \text{ m/s}$ , and  $10 \text{ m/s}$ , using droplets with a spherical diameter of  $D = 3 \text{ mm}$ . The initial state of droplet movement is marked as  $t = 0 \text{ ms}$ , with the red arrow indicating the direction of droplet movement along the tilted surface.



**Figure 8.** Schematic diagram of droplet with spherical diameter  $D = 3$  mm along the inclined windshield surface at different airflow speeds: (a)  $U = 3$  m/s; (b)  $U = 6$  m/s; (c)  $U = 10$  m/s.

As shown in the Figure 8, at  $U = 3$  m/s, the droplet retains its spherical cap shape in the initial state. Over time, the droplets travel greater distances along the surface and increase in velocity. At  $U = 6$  m/s, the droplet initially moves down the surface, but its contour changes significantly during movement, resulting in an increase in droplet height  $H$  and a decrease in wetting length  $L_d$ . Additionally, the distance the droplet travels decreases significantly between  $t = 100$  ms and 150 ms. At  $U = 10$  m/s, the high airflow velocity prevents the droplet from maintaining a symmetric spherical cap shape in the initial state, causing the droplet to accelerate upwards along the inclined plane.

In addition, this section also compares the profiles of droplets and the displacement of the contact line under airflow conditions of  $U = 6$  m/s between experimental observations and simulation results to validate the accuracy of the simulation. The distances between the contact lines in both experimental and numerical simulations were analyzed using the contact angle plug-in of ImageJ 1.8.0 software, with each measurement repeated five times for enhanced precision.

Figure 9a presents a comparison between the profiles of droplets in numerical simulations and experimental observations over various time intervals. Figure 9b depicts the movement distances of the advancing and receding contact lines. The average error between the numerical simulation results and the experimental measurements of the contact angle is found to be less than 5%, which falls within the acceptable range of engineering error. This demonstrates the reliability of the numerical model, as evidenced by the consistent agreement between the experimental data and the numerical results.

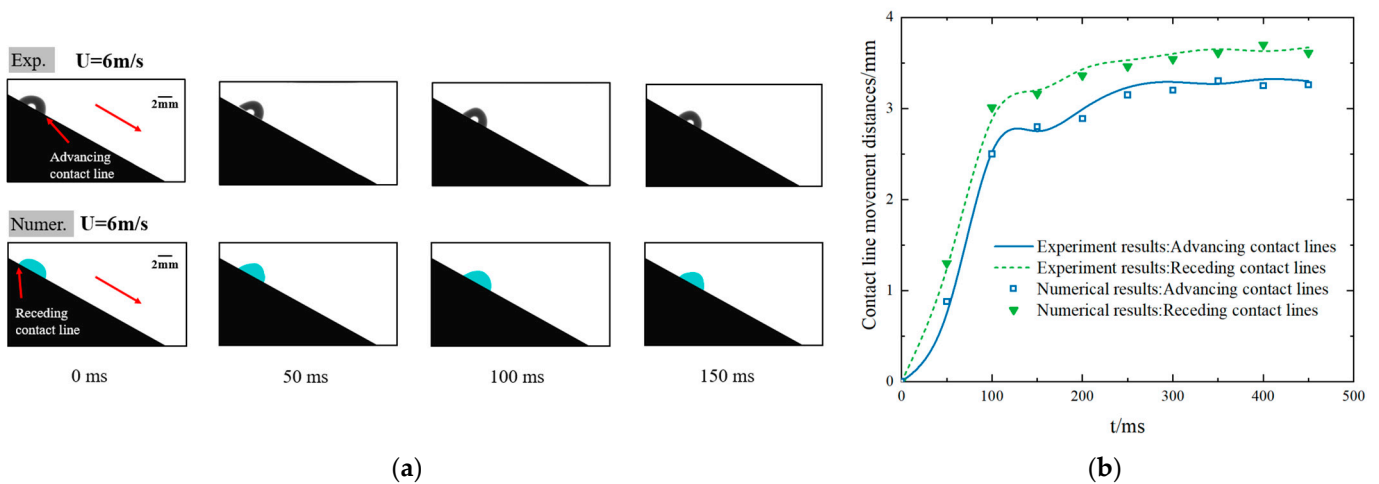


**Figure 9.** Comparison of the experiment and numerical stimulation results on the movement of a droplet under airflow: (a) Evolution of the droplet’s contours; (b) Evolution of the advancing and receding contact lines.

### 3.2. Forces Acting on the Droplet

Firstly, the droplet motion on the windshield should be deduced from the force analysis in the airflow. In the presence of the airflow, the droplets originally attached to the wall begin to deform, causing the advancing contact angle  $\theta_{adv}$  along the direction of motion to increase above the static contact angle  $\theta_e$ . The receding contact angle  $\theta_{rec}$  on the side away from the direction of motion decreases. The contact angle hysteresis force  $F_{adh}$  resulting from this phenomenon can be expressed as a function of the droplet wetting length  $L_d$ , the surface tension of the droplet  $\sigma$ , and the contact angle hysteresis [41].

$$F_{adh} = KL_d\sigma(\cos\theta_{rec} - \cos\theta_{adv}) \quad (20)$$

where  $K$  is denoted as an adjustable parameter describing the variation of the droplet contact line. According to the study of Rosiman et al. [15], the value of  $K$  is set as 1.

When a droplet moves rapidly on the windshield, there is internal friction in the droplet, which forms a resistance to motion. The internal flow field is rotating [42,43]. The rotating flow field and the mean flow field inside the droplet can overlap each other, which will form a boundary layer of thickness  $\delta$ . When the droplet diameter is larger than the capillary length  $\sqrt{\frac{\sigma}{\rho g}}$ , the viscous dissipation force  $F_\tau$  generated by the shear stress associated with the main part of the droplet will dominate the viscous dissipation. The viscous dissipation force  $F_\tau$  of the droplet is determined by the velocity gradient inside the droplet. According to the modification of the droplet velocity model proposed by Wang and Zhao [44], the viscous dissipation force  $F_\tau$  of the droplet will be improved as:

$$F_\tau = \mu A \frac{\partial u}{\partial y} = \mu A \frac{U_d \sqrt{Re}}{\sqrt{r \Delta y}} = \mu U_d V'^{\frac{1}{3}} \sqrt{Re} c_4(\theta_e) \quad (21)$$

where the Reynolds number  $Re$  is given by  $Re = \frac{\rho_l U_d r}{\mu}$ , where  $\rho_l$  is the density of water,  $U_d$  is the velocity of droplet, and  $r$  is half of the wetting length  $L_d$ ,  $r = L_d/2$ .

The geometric parameters describing the shape and motion of the droplet, such as the droplet volume  $V'$ , the contact area  $A$  between the droplet and the inclined surface, and the droplet motion velocity  $u$ , are brought into the expression for the viscous dissipative

force  $F_\tau$  of the droplet. It is necessary to introduce the expression  $c_4(\theta_e)$  for the equilibrium contact angle  $\theta_e$ .

$$c_4(\theta_e) = \frac{A}{V^{\frac{1}{3}}\sqrt{r\Delta y}} = \pi\left(\frac{3}{\pi}\right)^{\frac{1}{3}}\left(\frac{\sin^3\theta_e}{2-3\cos\theta_e+\cos^3\theta_e}\right)^{\frac{1}{2}}\left(\frac{2+\cos\theta_e}{1-\cos\theta_e}\right)^{\frac{1}{6}} \quad (22)$$

The wind direction is parallel to the windshield, so there is a certain wind traction force  $F_{wind}$  when the droplet moves on the windshield, which is defined by the equation:

$$F_{wind} = \frac{1}{2}\rho_g C_D S U^2 \quad (23)$$

where  $\rho_g$  is the air density,  $C_D$  is the drag coefficient,  $S$  is the projected area of the droplet, and  $U$  is the velocity of the airflow. The value of the drag coefficient  $C_D$  is related to the droplet shape and Reynolds number in the airflow. In order to improve the efficiency of calculation, the drag coefficient  $C_D$  of the rigid sphere model is set as 0.4.

As shown in Figure 10, the droplet attached to the windshield will be subjected to four forces when moving, namely, its own gravity  $F_g$ , droplet contact angle hysteresis  $F_{adh}$ , viscous dissipation force  $F_\tau$  and wind traction force  $F_{wind}$ . The directions of  $F_{adh}$  and  $F_\tau$  are both opposed to the direction of droplet motion.

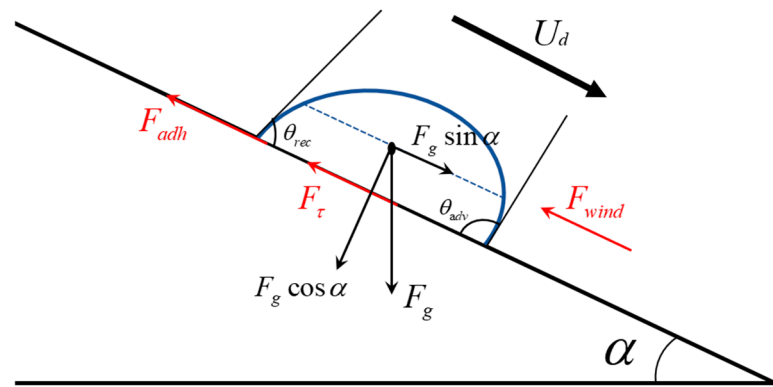


Figure 10. Force diagram of droplets in the airflow of downward motion in the windshield.

It can be shown from the force analysis that  $F_{adh}$ ,  $F_\tau$  and,  $F_{wind}$  are the key factors affecting the motion pattern of droplets under airflow. As the wind traction force  $F_{wind}$  increases, the direction of motion and acceleration of the droplet will change. Figure 11 shows the schematic diagram of the initial shape of the droplet moving in different directions along the surface of the windshield under the airflow.

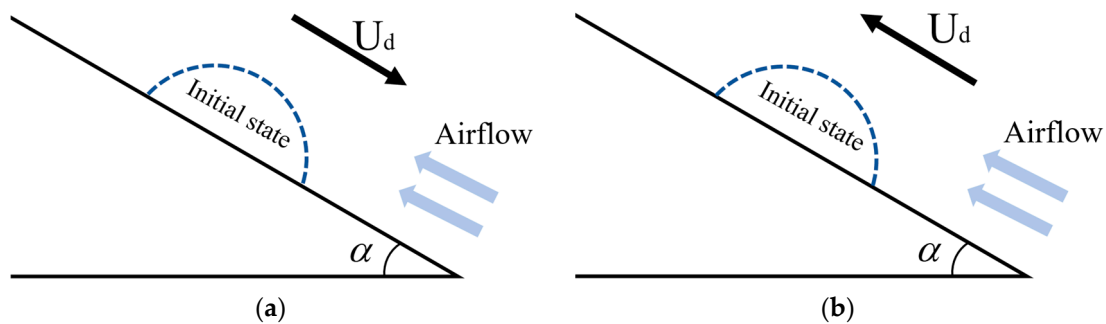


Figure 11. Schematic diagrams of droplets moving in different directions: (a) Upward; (b) Downward.

### 3.3. Motion Patterns of Droplets

In order to further understand the different dynamic behaviors of droplets on an inclined surface in the airflow, this section summarizes different motion patterns of droplets

by analyzing the changes in droplet contours. The experimental results in the previous section indicate that the droplet's direction will change as airflow velocity increases. To better capture and analyze this change in droplet morphology and movement pattern in an airflow environment, this study reproduces the movement of the surface droplet through planarization, and the direction of the droplet's movement is indicated by the arrows in the picture.

The changes in droplet contours at different times on a 30° windshield for droplets with a spherical diameter  $D$  of 3 mm, 3.5 mm, and 4 mm in air velocities  $U$  of 3–7 m/s are illustrated in Figure 12.  $t = 0$  corresponds to the beginning of droplet motion. The initial state of the droplet is a spherical cap shape. As time increases, the droplet profiles begin to change. From the overall view of Figure 12, the droplet motion direction is all downward along the windshield. In the states of air velocity  $U$  of 3 m/s and 4 m/s, the influence of airflow is smaller, and the droplet still shows a tendency to accelerate downward. With the increase in droplet size, the inertia force of droplet motion is enhanced, resulting in the increasing speed of droplet motion. The deformation effects of the droplet are also more obvious, which are manifested by a larger advancing contact angle  $\theta_{adv}$  and a smaller receding contact angle  $\theta_{rec}$ . When the droplets are the same size, with the increase in wind speed, the droplets slide down the inclined surface with a decreasing distance, the wetting length  $L_d$  decreases with the increase of the droplet height  $H$ , the advancing contact angle  $\theta_{adv}$  decreases and the receding contact angle  $\theta_{rec}$  increases.

However, when the wind speed is increased to 7 m/s, it can be seen from the schematic diagrams of the droplet contours that the sliding distance of the droplet decreases for the same time span. The profiles of 3 mm droplets at  $t = 100$  ms and  $t = 150$  ms are approximately coincident, and there is also a tendency for the profiles of 3.5 mm and 4 mm droplets to coincide. This means that, when the wind speed increases to a certain value, the movement speed of the droplets shows an increase and then decreases, and may even have a stationary tendency.

To obtain the motion of droplets on the windshield at higher air speeds, Figure 13 illustrates the variation of the profiles of  $D = 3$  mm, 3.5 mm, and 4 mm droplets at different times on a 30° windshield in air velocity  $U$  of 8–12 m/s. It can be seen from Figure 13 that the direction of the droplets is upwards along the inclined plane. At wind speed of 8 m/s, the 3 mm droplet accelerated to climb along the inclined surface, the droplet contours of 3.5 mm and 4 mm overlapped after climbing for a certain distance, and the velocity first increased and then decreased. With increasing air velocity, which makes the wind traction force  $F_{wind}$  dominant, the phenomenon of accelerated droplet climbing is more obvious, and the degree of droplet profile changes is more drastic. With the increase in droplet sizes, the inertia force of the droplet increases, and the increase in droplet velocity in the same time is greater. Even the rear part of the 3.5 mm and 4 mm droplets formed a “tail” at higher wind speeds, in which case the receding contact angle  $\theta_{rec}$  of the droplets decreased significantly and the wetting length  $L_d$  increased significantly.

In summary, when the wind speed increases, the droplets originally adhering to the slant surface show different motion patterns, which can be summarised into three main states: in the first state, the wind speed is small, the droplets are mainly driven by the gravity force  $F_g \sin \alpha$ , and the droplets will accelerate along the slant surface. In the second state, with increase in the wind speed, the droplets begin to tend to remain static and, due to the change of morphology, the droplets are balanced by the force. In the third state, in the environment of larger wind speed, the adherent droplets will be accelerated upward along the inclined plane dominated by the wind traction force  $F_{wind}$ , and the morphology of the droplets will change significantly with time during the movement.

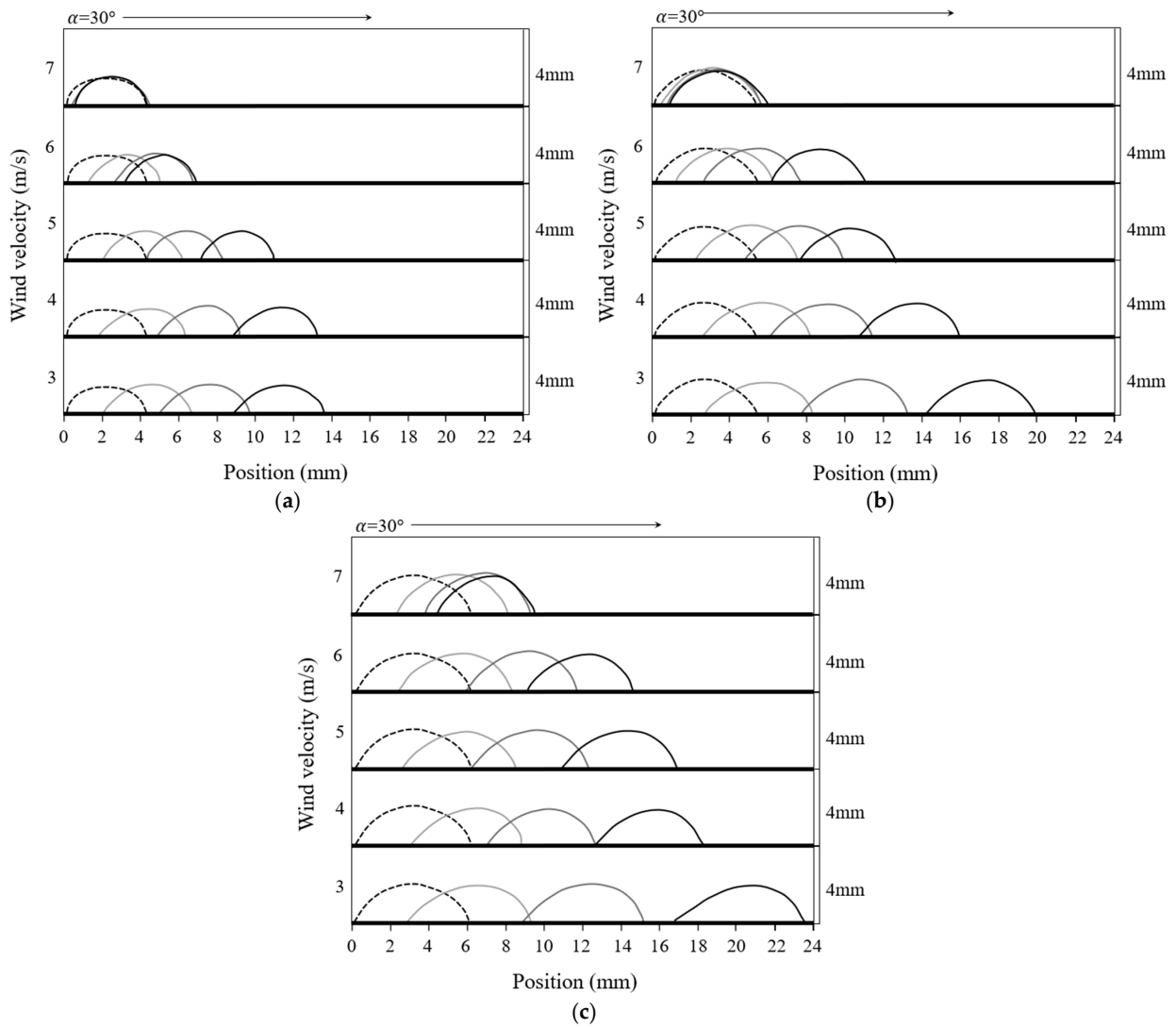


**Figure 12.** Schematic diagrams of droplet contours and motion on the windshield at air velocity  $U$  of 3–7 m/s: (a)  $D = 3$  mm; (b)  $D = 3.5$  mm; (c)  $D = 4$  mm; (The arrow direction corresponds to the direction of droplet motion, and the contours correspond to the time step: 0 s–50 ms–100 ms–150 ms).

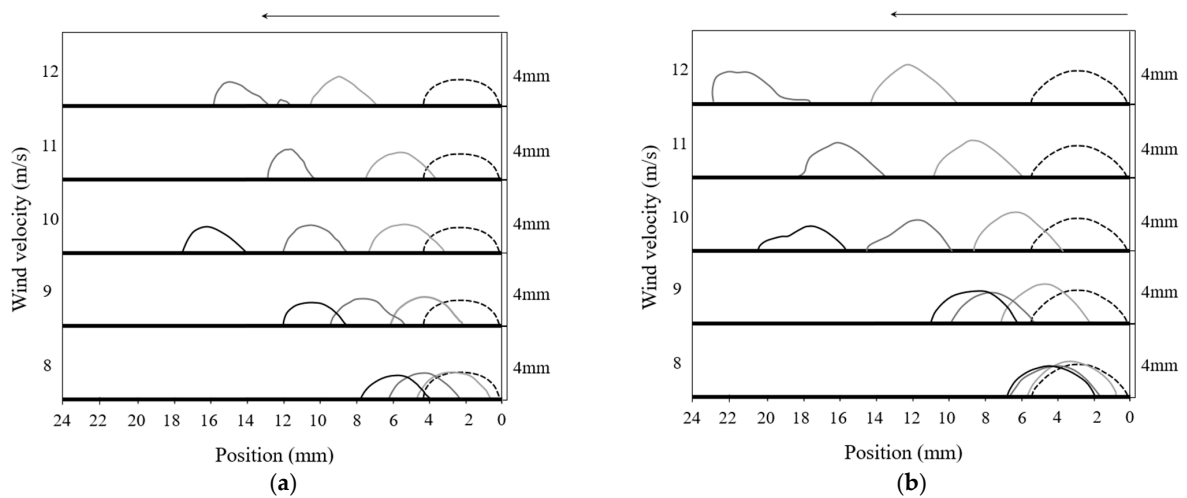


**Figure 13.** Cont.

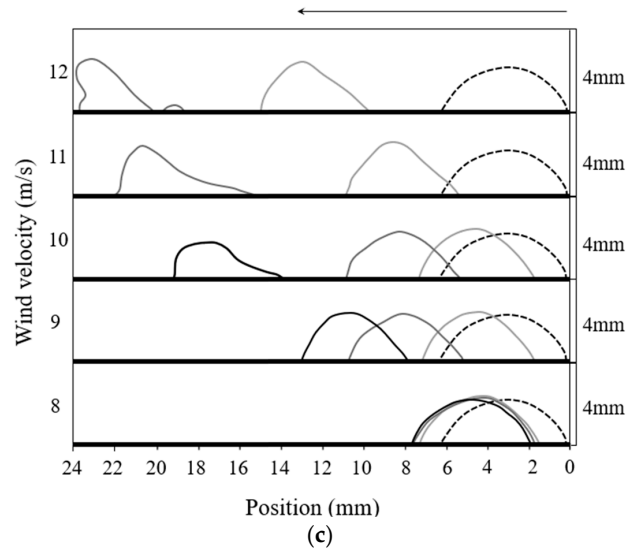


**Figure 13.** Schematic diagrams of droplet contours and motion on the windshield at air velocity  $U$  of 8–12 m/s: (a)  $D = 3$  mm; (b)  $D = 3.5$  mm; (c)  $D = 4$  mm; (The arrow direction corresponds to the direction of droplet motion, and the contours correspond to the time step: 0 s–50 ms–100 ms–150 ms).

### 3.4. Changes in Droplet Morphology Parameters

Based on the above analysis, it has been concluded that, under different air velocities, the adhering droplets on the inclined surface can be divided into three motion modes: accelerated decline, force equilibrium, and accelerated climb. In this section, the surface wettability and surface properties of droplets under different motion modes are described by investigating the droplet wetting length  $L_d$ , droplet height  $H$ , and the cosine number of advancing contact angle  $\theta_{adv}$  and receding contact angle  $\theta_{rec}$  on the inclined surface.

Figure 14 compares the values of wetting length  $L_d$  and droplet height  $H$  in different motion modes for the adherent droplets with spherical diameter  $D$  of 3 mm, 3.5 mm, and 4 mm on a  $30^\circ$  windshield in the air velocity of  $U = 3$  m/s, 7 m/s and 10 m/s based on the simulation results in the previous section. From Figure 14a,b, at the velocity of  $U = 3$  m/s, the droplet is in an accelerated downward motion at this time. The gravitational component force  $F_g \sin \alpha$  dominates the droplet motion. Therefore, the value of wetting length  $L_d$  will be affected by the dominant force at the beginning, and then increased, while the value of droplet height  $H$  will decrease. As the size of the droplet increases, the inertial force of the droplet strengthens, leading to a more pronounced increase in  $L_d$  and decrease in  $H$ . The forces gradually stabilize the droplet during the continuous acceleration of the decline. Therefore, the droplet morphology also reflects the trend of  $L_d$  and  $H$  changes first and then stabilizes. However, due to the existence of constant output wind force and the inertial force, it will lead to the oscillation at the droplet interface, and the value of  $L_d$  and  $H$  have smaller fluctuations under this trend. At wind speed  $U = 7$  m/s, wind traction force  $F_{wind}$  increases significantly. From Figure 14c,d, unlike the case of  $U = 3$  m/s, the value of  $L_d$ , which initially adheres to the inclined surface and remains stable, decreases significantly, and the value of  $H$  increases significantly, showing a “compact” droplet pattern. At this time, the droplet forces have not yet reached equilibrium, so in the subsequent motion process the force equilibrium will be reached through the change in  $L_d$  and  $H$ . With time changes, the value of  $L_d$  increases and tends to be stable, but the value of  $H$  still fluctuates up and down, and gradually stabilizes after 120 ms. From the overall tendency, the stable value of  $L_d$  decreases and the value of  $H$  increases compared with the initial value.

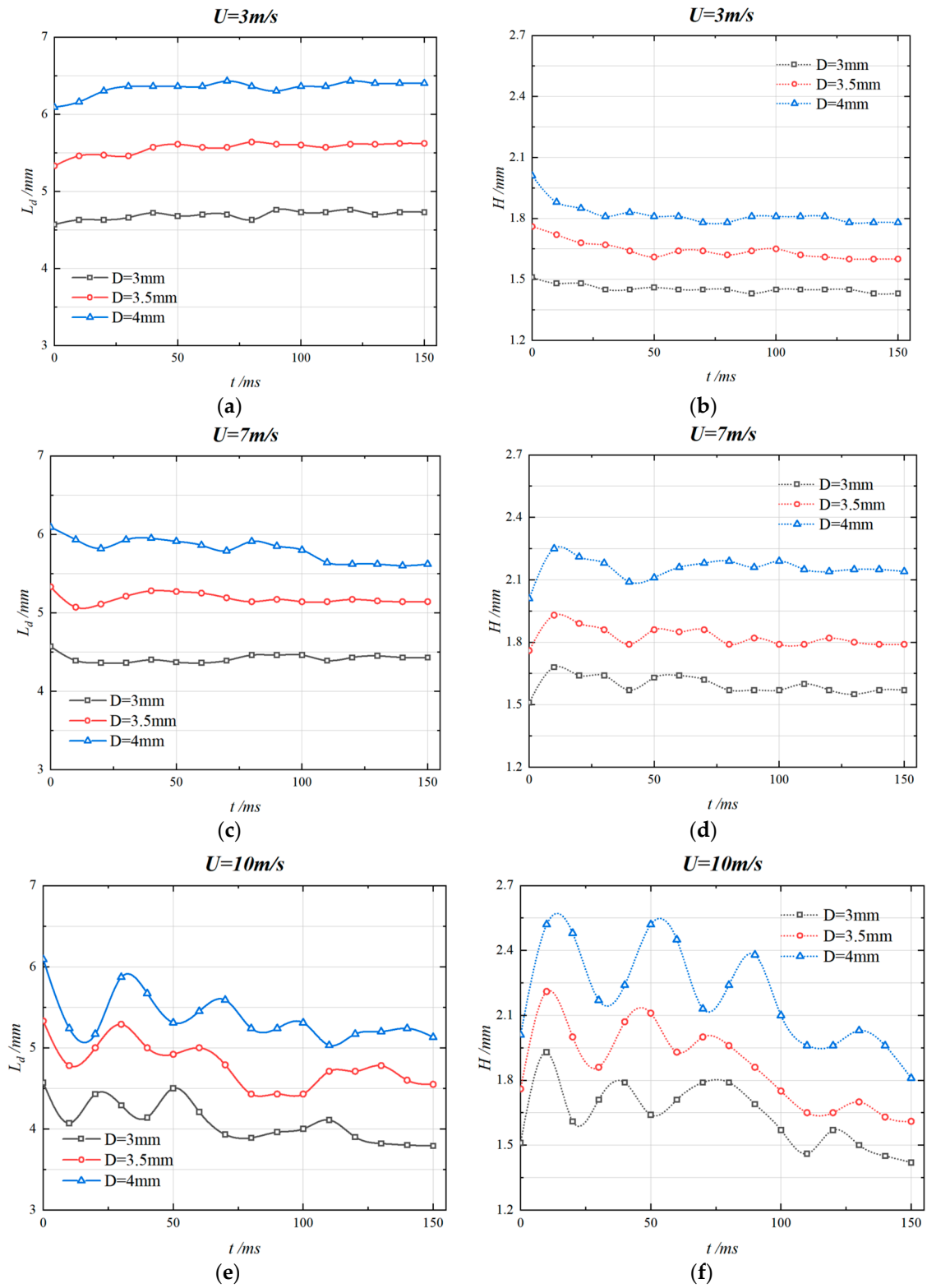


**Figure 14.** Diagrams of droplet wetting length  $L_d$  and droplet height  $H$  with initial spherical diameters  $D$  of 3 mm, 3.5 mm and 4 mm in different air velocities: (a,b)  $U = 3 \text{ m/s}$ ; (c,d)  $U = 7 \text{ m/s}$ ; (e,f)  $U = 10 \text{ m/s}$ .

At higher wind speeds  $U = 10 \text{ m/s}$ , at this time wind traction force  $F_{wind}$  becomes completely the dominant force in the droplet motion. From Figure 14e,f, it can be seen that, the higher the wind speed, the more likely the droplets will experience violent interfacial oscillations. Therefore, raindrops experience sharp changes in both droplet wetting length

$L_d$  and droplet height  $H$  values during the climb along the inclined plane, and this change increases as the size of the droplet increases. At the moment of initial motion, the droplets are more “compact” than at  $U = 7$  m/s due to the influence of larger airflow force, and the number and amplitude of fluctuations in the  $L_d$  and  $H$  values are much higher. Before  $t = 100$  ms, the direction of  $L_d$  and  $H$  fluctuations also shows a completely opposite trend. However, at  $t = 150$  ms, the  $L_d$  and  $H$  values are lower than the initial values, probably due to the excessive wind speed that causes the droplets to climb too far and leave some liquid in their wake.

Figure 15 shows the cosine number of advancing contact angle  $\theta_{adv}$  and receding contact angle  $\theta_{rec}$  of the initially spherical diameters  $D$  of 3 mm, 3.5 mm, and 4 mm adherent droplets on the inclined surface at the speed of  $U = 3$  m/s and 7 m/s. From Figure 15a, the cosine component of the advancing contact angle  $\theta_{adv}$  decreases and then stabilizes with time, while the cosine component of the receding contact angle  $\theta_{rec}$  increases and then stabilizes. Moreover, the increase and decrease in the cosine component of the contact angle can be more obvious with larger droplet sizes, because the droplet on the inclined surface is affected by the gravitational force, which causes continuous deformation of the droplet shape, and the contact angle of the droplet is stabilized after the force is stabilized. The results of contact angle at wind speed of 7 m/s are shown in Figure 15b. Initially, the change in the cosine component of contact angle is similar to that at 3 m/s when the droplet is not in equilibrium. However, after  $t = 100$  ms, the cosine values of the droplet advancing  $\theta_{adv}$  and receding contact angles  $\theta_{rec}$  tend to be close to each other, which makes the droplet contact angle hysteresis reduce and promotes the droplet force equilibrium.

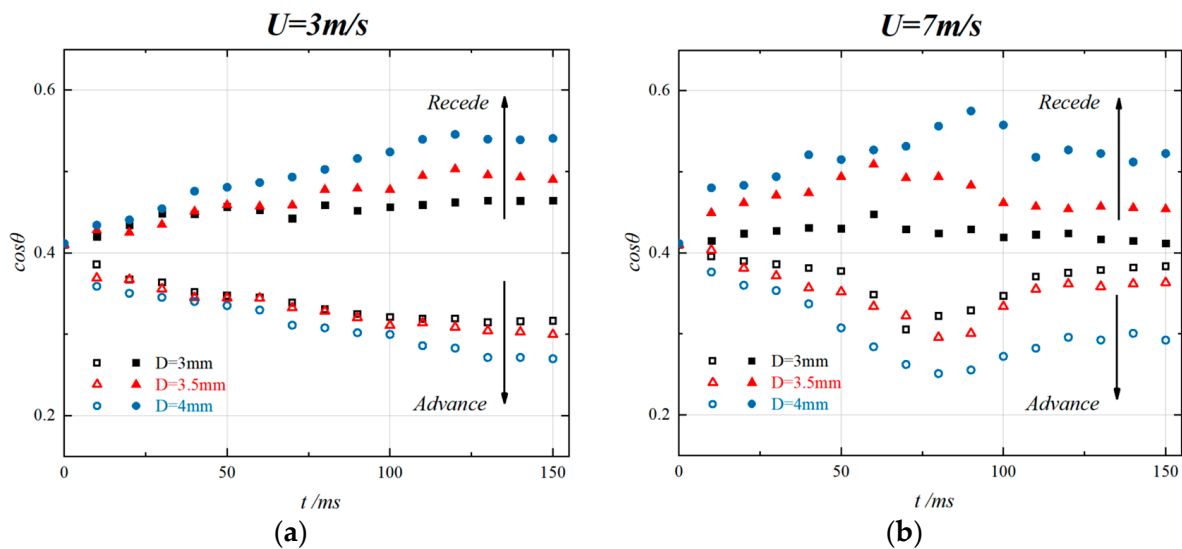


**Figure 15.** Variations of contact angle cosine for droplets with initial spherical diameter  $D$  of 3 mm, 3.5 mm and 4 mm in different air velocities: (a)  $U = 3$  m/s; (b)  $U = 7$  m/s.

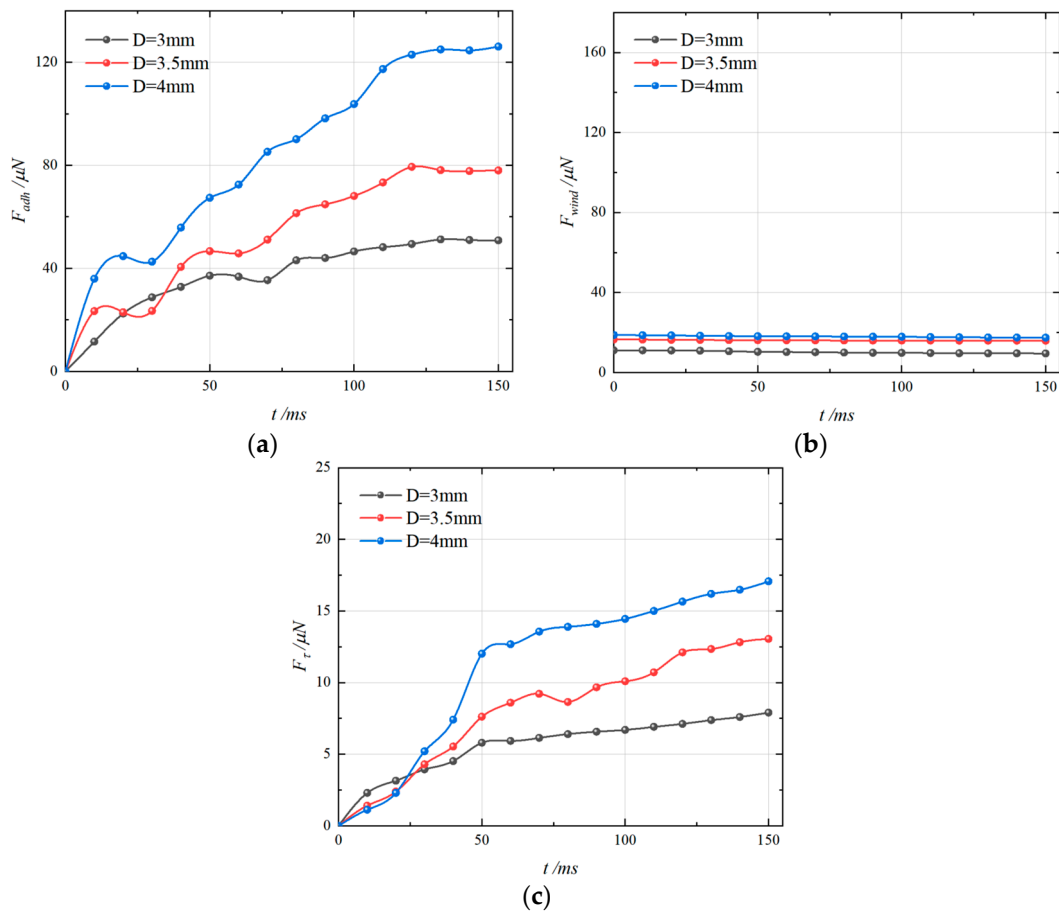
### 3.5. Dynamic Force Analysis

To further understand the impact of changes in size and airflow velocity on the motion state of droplets, this section provides quantitative results of droplet contact angle hysteresis force  $F_{adh}$ , viscous dissipation force  $F_{\tau}$ , and wind traction force  $F_{wind}$ , comparing and discussing the magnitude of the droplet motion dominant force and the sum of other component forces.

#### 3.5.1. Impact of Droplet Sizes

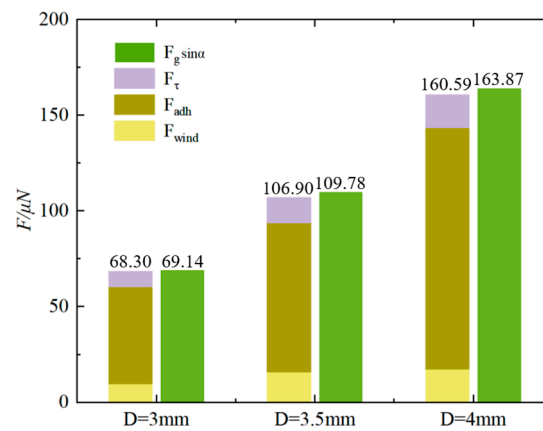
Figure 16 illustrates the variations in force experienced by droplets of sizes  $D = 3$  mm,  $D = 3.5$  mm, and  $D = 4$  mm under the airflow of  $U = 3$  m/s. The evolution of the droplet contact angle hysteresis force  $F_{adh}$ , a significant factor impeding droplet movement, is

depicted in Figure 16a. According to Equation (20), the primary determinants are the differences in cosine values of the advancing and receding contact angles  $\cos\theta_{rec} - \cos\theta_{adv}$ , and the wetting length  $L_d$ . As the droplet size increases, the wetting length  $L_d$  also increases. The analysis of the cosine values of the contact angles in Figure 15a reveals that an increase in the advancing contact angle  $\theta_{adv}$ , and a decrease in the receding contact angle  $\theta_{rec}$ , which lead to a rise in the value of  $\cos\theta_{rec} - \cos\theta_{adv}$  over time. Moreover, as the droplet size enlarges, the initial fluctuation effect during droplet movement becomes more pronounced. Consequently, with the passage of time and increase in droplet size, the value of  $F_{adh}$  escalates, and the initial fluctuations in droplet movement become more evident. Under the influence of airflow, the wind traction force  $F_{wind}$  exerted on the droplet is illustrated in Figure 16b. The figure indicates that, at low airflow speeds,  $F_{wind}$  is generally modest, but its magnitude escalates with droplet size increases. According to Equation (23),  $F_{wind}$  is primarily influenced by the airflow velocity and the projected area  $S$  of the droplet. At the same airflow speed, an increase in the wetting length  $L_d$  of the droplet during its movement leads to a slight decrease in its the projected area, resulting in a decrease in the  $F_{wind}$ . The viscous dissipation force  $F_{\tau}$  of the droplet, determined by the internal velocity gradient, is depicted in Figure 16c. The figure shows that, with the progression of time and enlargement of droplet size, the rate of increase of the viscous dissipation force  $F_{\tau}$  initially rises and then diminishes, because the magnitude of the viscous dissipation force  $F_{\tau}$  is mainly influenced by the volume of the droplet and the speed of its movement. As the droplet size expands, its volume increase. In the airflow of  $U = 3$  m/s, the droplet accelerates its slide along the surface, resulting in a continuous increase in its speed.



**Figure 16.** Evolution of the force magnitude on droplets of different sizes over time at  $U = 3$  m/s: (a) contact angle hysteresis force  $F_{adh}$ ; (b) wind traction force  $F_{wind}$ ; (c) viscous dissipation force  $F_{\tau}$ .

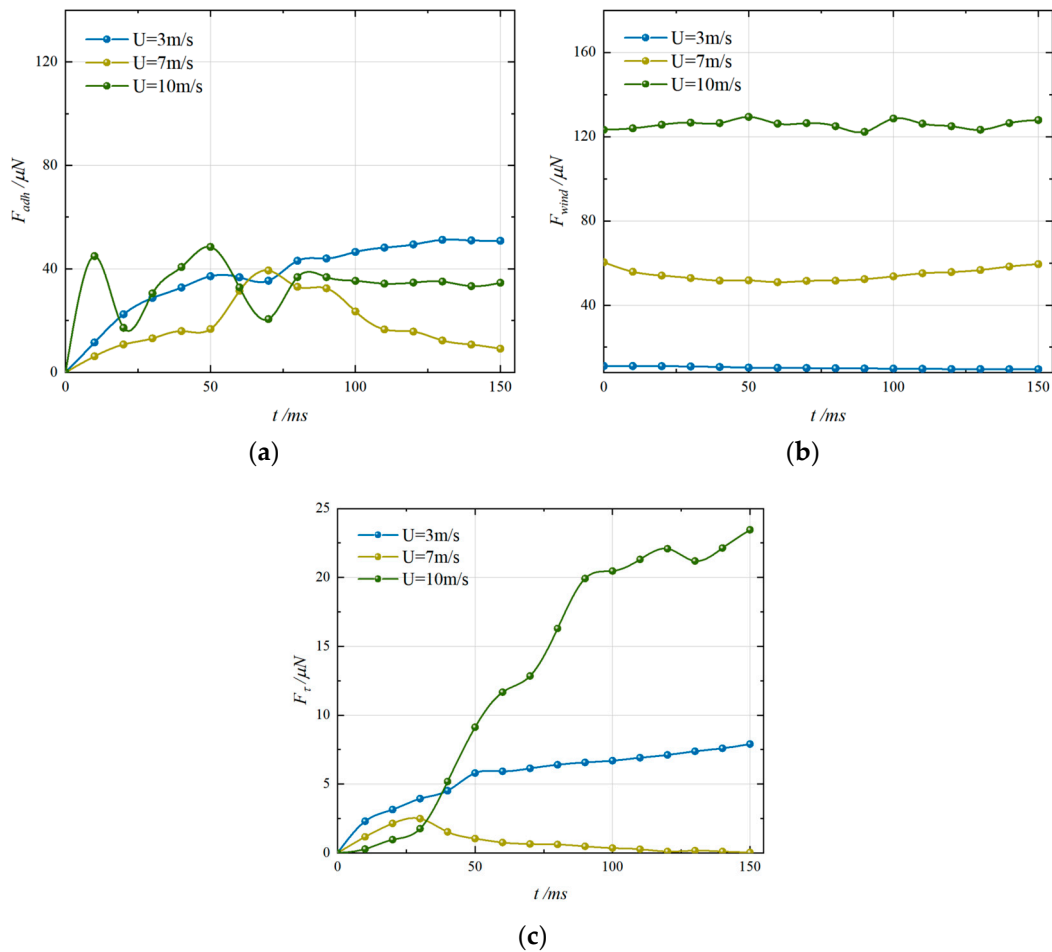
According to the analysis in Section 3.3, at the velocity of  $U = 3$  m/s, the droplet undergoes accelerated sliding motion, with its gravitational component  $F_g \sin \alpha$  serving as the primary force propelling the motion. In contrast, the contact angle hysteresis force  $F_{adh}$ , viscous dissipation force  $F_\tau$ , and wind traction force  $F_{wind}$  act as impediments. To illustrate the variations in forces acting on the droplets, Figure 17 displays a bar chart comparing the magnitude of the droplet's gravitational component force  $F_g \sin \alpha$  with the sum of the other inhibitory forces at  $t = 150$  ms. The force values are annotated on the bars. As depicted in the graph, the contact angle hysteresis force  $F_{adh}$  emerges as the most substantial force obstructing the droplet's motion. During the accelerated sliding phase, the droplet's gravitational component force marginally exceeds the aggregate of the contact angle hysteresis force  $F_{adh}$ , viscous dissipation force  $F_\tau$ , and wind traction force  $F_{wind}$ , aligning with the findings in Section 3.3. Additionally, as the droplet size progressively increases, the disparity between the gravitational component force and the sum of the other resisting forces also grows.



**Figure 17.** Comparison of the dominant force and the sum of hindering forces.

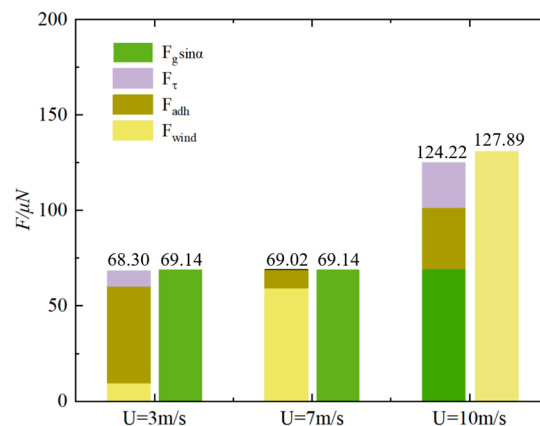
### 3.5.2. Impact of Air Velocities

Figure 18 illustrates the variations in force experienced by the droplet with a spherical diameter of  $D = 3$  mm under airflow velocities of  $U = 3$  m/s, 7 m/s, and 10 m/s. The evolution of the contact angle hysteresis force  $F_{adh}$  is depicted in Figure 18a. At  $U = 3$  m/s, during the accelerated sliding phase, the value of  $\cos \theta_{rec} - \cos \theta_{adv}$  increases, leading to a corresponding increase in  $F_{adh}$  over time. At  $U = 7$  m/s, the droplet undergoes initial acceleration followed by a halt, with the value of  $\cos \theta_{rec} - \cos \theta_{adv}$  first rising and then falling, mirroring the trend in  $F_{adh}$ . At  $U = 10$  m/s, the droplet accelerates upward, due to the impact of the airflow, and the droplet's shape undergoes significant alterations initially, causing fluctuations in the value of  $\cos \theta_{rec} - \cos \theta_{adv}$ . However, as the upward trajectory of the droplet stabilizes, the value of  $F_{adh}$  also stabilizes. Figure 18b shows the wind traction force  $F_{wind}$  of the droplet at different airflow velocities. It is evident that, as the airflow velocity escalates, the value of  $F_{wind}$  also increases. At higher wind speeds, the instability in the droplet's projected area  $S$  leads to fluctuations in the value of  $F_{wind}$ . Figure 18c presents the magnitude of the viscous dissipation force  $F_\tau$  acting on the droplet. Given that the volume of the droplet remains constant, the value of  $F_\tau$  aligns with the trend in the droplet's speed. With the increase in airflow velocity, the droplet's motion mode transitions from accelerated sliding to a state of force equilibrium, and eventually to accelerated climbing. In the accelerated sliding mode, the speed of the droplet progressively increases. In the force equilibrium mode, the speed initially rises and then decreases. In the accelerated climbing mode, the speed of the droplet consistently increases, with the direction opposite to that observed in the accelerated sliding mode.



**Figure 18.** Evolution of the force magnitude on droplets of  $D = 3\text{ mm}$  over time at different velocities: (a) contact angle hysteresis force  $F_{adh}$ ; (b) wind traction force  $F_{wind}$ ; (c) viscous dissipation force  $F_{\tau}$ .

As the airflow velocity changes, the dominant force influencing the droplet also changes. Figure 19 presents a bar chart comparing the dominant force with the sum of other hindering forces at different airflow velocities. The chart reveals that, at  $U = 3\text{ m/s}$  and  $U = 7\text{ m/s}$ , the gravitational component  $F_g \sin\alpha$  serves as the principal force driving the droplet. With an increase in airflow velocity, the total of other hindering forces also rises, nearing the value of  $F_g \sin\alpha$ . However, at  $U = 10\text{ m/s}$ , the leading force in the droplet shifts to  $F_{wind}$ , and the magnitude of  $F_{wind}$  surpasses the aggregate of other forces, propelling the droplet to accelerate upward in alignment with the airflow direction.



**Figure 19.** Comparison of the dominant force and the sum of hindering forces.

#### 4. Conclusions

In this study, the CLSVOF method is employed to examine the behavior of droplet adhesion on the inclined windshield surface under airflow. Droplet sizes and airflow velocities are considered as key factors influencing this phenomenon. Firstly, the study focuses on exploring the variations in the direction and displacement of droplets under different air velocities. Subsequently, based on the outcomes of the numerical simulations, a classification of the droplet motion patterns is established, and the trends in the changes of droplet morphological parameters are analyzed. Finally, the forces acting on the droplets are calculated using relevant equations. The temporal evolution of these forces is investigated, and the primary forces driving droplet movement are compared with other resisting forces.

At different airflow velocities, the wind traction force  $F_{wind}$  acting on the droplet changes, leading to distinct modes of droplet motion: accelerated sliding at low wind speeds, equilibrium of forces, and accelerated climbing at high speeds. When the wind speed is low, the gravitational component  $F_g \sin \alpha$  predominates in the droplet's movement, surpassing the combined effect of other impeding forces, causing the droplet to accelerate downwards along the surface. During this process, the wetting length  $L_d$  of the droplet increases, while its height  $H$  decreases slightly. The advancing contact angle  $\theta_{adv}$  increases, and the receding contact angle  $\theta_{rec}$  decreases, resulting in a larger difference in the cosine of the contact angles. As the size of the droplet increases, the variation in morphological parameters becomes more pronounced, and the disparity between the gravitational component  $F_g \sin \alpha$  and the sum of other hindering forces continues to grow.

In the force equilibrium mode, the velocity of the droplet initially increases and then decreases with the rise in air velocity. Throughout the movement, the wetting length  $L_d$  of the droplet diminishes while its height  $H$  escalates, resulting in a more compact droplet profile. The advancing contact angle  $\theta_{adv}$  initially rises and then falls, whereas the receding contact angle  $\theta_{rec}$  exhibits the opposite trend. The differences in the cosine values of the contact angle first increase and then decrease, mirroring the variation pattern of the contact angle hysteresis force  $F_{adh}$ .

When the airflow velocity is high, the droplet accelerates along the surface, primarily driven by wind traction force  $F_{wind}$ . As the velocity of the droplet increases, the value of the viscous dissipation force  $F_\tau$  also rises. In this mode of motion, the wind traction force  $F_{wind}$  exceeds the combined value of other forces that impede the droplet's movement. During this phase, the droplet's interface experiences intense oscillations, leading to significant fluctuations in both the wetting length  $L_d$  and the height  $H$  of the droplet. In addition, the value of  $F_{adh}$  and  $F_{wind}$  also exhibits substantial variations because of droplet oscillation.

If the inclination angle of the windshield and the state of the liquid falling change, the behavior of the droplets will also change. Therefore, to understand the droplet motion behavior on the window surface in more detail, further studies are needed based on different droplet falling states and inclination angles of the windshield, which will be the next step in the study.

**Author Contributions:** Conceptualization, F.D. and L.X.; methodology L.X.; software, X.X.; validation, X.X. and L.X.; formal analysis, F.D.; investigation, X.X. and L.X.; resources, F.D.; data curation, X.X.; writing—original draft preparation, X.X.; writing—review and editing, X.X.; visualization, L.X.; supervision, F.D.; project administration, F.D.; funding acquisition, F.D. All authors have read and agreed to the published version of the manuscript.

**Funding:** This research was funded by Industry Foresight and Key Core Technology Carbon Dafeng Carbon Neutral Science and Technology Innovation Special Funds, grant number BE2023091-1.

**Institutional Review Board Statement:** Not applicable.

**Informed Consent Statement:** Not applicable.

**Data Availability Statement:** The data presented in this study are available on request from the corresponding author.

**Conflicts of Interest:** The authors declare no conflicts of interest.

## References

1. Li, H.; Yu, S. A robust superhydrophobic surface and origins of its self-cleaning properties. *Appl. Surf. Sci.* **2017**, *420*, 336–345. [[CrossRef](#)]
2. Zhang, K.; Li, Z.; Macey, M.; Chen, S.; Karniadakis, G.E. Self-cleaning of hydrophobic rough surfaces by coalescence-induced wetting transition. *Langmuir* **2019**, *35*, 2431–2442. [[CrossRef](#)]
3. Jin, Z.; Mei, H.; Pan, L.; Liu, H.; Cheng, L. Superhydrophobic self-cleaning hierarchical micro-/nanocomposite coating with high corrosion resistance and durability. *ACS Sustain. Chem. Eng.* **2021**, *9*, 4111–4121. [[CrossRef](#)]
4. Mandal, P.; Perumal, G.; Arora, H.S.; Ghosh, S.K.; Grewal, H.S. Green manufacturing of nanostructured Al-Based sustainable self-cleaning metallic surfaces. *J. Clean. Prod.* **2021**, *278*, 123373. [[CrossRef](#)]
5. Rioboo, R.; Tropea, C.; Marengo, M. Outcomes from a drop impact on solid surfaces. *At. Sprays* **2001**, *11*, 12. [[CrossRef](#)]
6. Marengo, M.; Antonini, C.; Roisman, I.V.; Tropea, C. Drop collisions with simple and complex surfaces. *Curr. Opin. Colloid Interface Sci.* **2011**, *16*, 292–302. [[CrossRef](#)]
7. Chung, J.; Lee, K.; Lee, C.-H.; Kong, N. Clamping performance of fastener in windshield wiper assembly using theoretical and experimental methods. *Int. J. Automot. Technol.* **2016**, *17*, 99–107. [[CrossRef](#)]
8. Huang, T.C.; Tsai, J.W.; Liao, K.C. Geometry Optimization of a Metallic Flexor for Flat Wipers. *Int. J. Automot. Technol.* **2021**, *22*, 823–830. [[CrossRef](#)]
9. Zolfagharian, A.; Ghasemi, S.E.; Imani, M. A multi-objective, active fuzzy force controller in control of flexible wiper system. *Lat. Am. J. Solids Struct.* **2014**, *11*, 1490–1514. [[CrossRef](#)]
10. Lee, K.-E.; Chen, X.-Z.; Yu, C.-W.; Chin, K.-Y.; Wang, Y.-C.; Hsiao, C.-Y.; Chen, Y.-L. An intelligent driving assistance system based on lightweight deep learning models. *IEEE Access* **2022**, *10*, 111888–111900. [[CrossRef](#)]
11. Yasmeen, S.; Yoon, J.; Moon, C.H.; Khan, R.; Gaiji, H.; Shin, S.; Oh, I.-K.; Lee, H.-B.-R. Self-formation of superhydrophobic surfaces through interfacial energy engineering between liquids and particles. *Langmuir* **2021**, *37*, 5356–5363. [[CrossRef](#)] [[PubMed](#)]
12. Feng, X.; Shi, Y.; Yin, X.; Wang, X. Transparent superhydrophobic film with anti-fouling and anti-scaling ability by facile method of dip-coating SiO<sub>2</sub> Sol. *Mater. Res. Express* **2022**, *9*, 016404. [[CrossRef](#)]
13. Lyu, J.; Wu, B.; Wu, N.; Peng, C.; Yang, J.; Meng, Y.; Xing, S. Green preparation of transparent superhydrophobic coatings with persistent dynamic impact resistance for outdoor applications. *Chem. Eng. J.* **2021**, *404*, 126456. [[CrossRef](#)]
14. Milne, A.; Amirfazli, A. Drop shedding by shear flow for hydrophilic to superhydrophobic surfaces. *Langmuir* **2009**, *25*, 14155–14164. [[CrossRef](#)] [[PubMed](#)]
15. Roisman, I.V.; Criscione, A.; Tropea, C.; Mandal, D.K.; Amirfazli, A. Dislodging a sessile drop by a high-Reynolds-number shear flow at subfreezing temperatures. *Phys. Rev. E* **2015**, *92*, 023007. [[CrossRef](#)] [[PubMed](#)]
16. Barwari, B.; Burgmann, S.; Bechtold, A.; Rohde, M.; Janoske, U. Experimental study of the onset of downstream motion of adhering droplets in turbulent shear flows. *Exp. Therm. Fluid Sci.* **2019**, *109*, 109843. [[CrossRef](#)]
17. Hooshanginejad, A.; Lee, S. Droplet depinning in a wake. *Phys. Rev. Fluids* **2017**, *2*, 031601. [[CrossRef](#)]
18. Razzaghi, A.; Amirfazli, A. Shedding of a pair of sessile droplets. *Int. J. Multiph. Flow* **2019**, *110*, 59–68. [[CrossRef](#)]
19. Rohde, M.; Barwari, B.; Burgmann, S.; Janoske, U. Droplet motion induced by superposition of shear flow and horizontal surface vibration. *Int. J. Multiph. Flow* **2022**, *155*, 104163. [[CrossRef](#)]
20. Yeganehdoust, F.; Hanson, J.; Johnson, Z.; Jadidi, M.; Moghtadernejad, S. Experimental and numerical analysis of shear-driven droplet coalescence on surfaces with various wettabilities. *Phys. Fluids* **2023**, *35*, 022110. [[CrossRef](#)]
21. Shi, T.; Yang, H.; Peng, H.; Xia, Z. Droplet shedding on hydrophilic and superhydrophobic surfaces under the effect of air shear flow. *J. Coat. Technol. Res.* **2024**, *21*, 789–798. [[CrossRef](#)]
22. Hashimoto, A.; Sakai, M.; Song, J.-H.; Yoshida, N.; Suzuki, S.; Kameshima, Y.; Nakajima, A. Direct observation of water droplet motion on a hydrophobic self-assembled monolayer surface under airflow. *J. Surf. Finish. Soc. Jpn.* **2008**, *59*, 907. [[CrossRef](#)]
23. Nakata, N.; Kakimoto, M.; Nishita, T. Animation of water droplets on a hydrophobic windshield. In Proceedings of the WSCG 2012: 20th International Conference on Computer Graphics, Visualization and Computer Vision 2012, Plzen, Czech Republic, 25–28 June 2012.
24. Chen, K.-C.; Chen, P.-S.; Wong, S.-K. A hybrid method for water droplet simulation. In Proceedings of the 11th ACM SIG-GRAPH International Conference on Virtual-Reality Continuum and Its Applications in Industry, Singapore, 2–4 December 2012; pp. 341–344.
25. Koblik, K. Simulation of Rain on a Windshield: Creating a Real-Time Effect Using GPGPU Computing. Master's Thesis, Umeå University, Umeå, Sweden, 2021.
26. White, E.B.; Schmucker, J.A. Wind-and gravity-forced drop depinning. *Phys. Rev. Fluids* **2021**, *6*, 023601. [[CrossRef](#)]
27. Hu, H.; Lai, Z.; Hu, C. Droplet shedding characteristics on metal fibers with different wettability and inclined angles. *Int. J. Refrig.* **2021**, *130*, 271–277. [[CrossRef](#)]
28. Yurishchev, A.; Ullmann, A.; Brauner, N. Experiments and modeling of droplets motion induced by turbulent air flow on inclined surfaces. *Exp. Therm. Fluid Sci.* **2023**, *140*, 110763. [[CrossRef](#)]
29. Conan, B.; Anthoine, J.; Planquart, P. Experimental aerodynamic study of a car-type bluff body. *Exp. Fluids* **2011**, *50*, 1273–1284. [[CrossRef](#)]
30. Mahrous, E.; Roy, R.V.; Jarauta, A.; Secanell, M. A two-dimensional numerical model for the sliding motion of liquid drops by the particle finite element method. *Phys. Fluids* **2021**, *33*, 032117. [[CrossRef](#)]

31. Guildenbecher, D.; López-Rivera, C.; Sojka, P. Secondary atomization. *Exp. Fluids* **2009**, *46*, 371–402. [[CrossRef](#)]
32. Osher, S.; Fedkiw, R.P. Level set methods: An overview and some recent results. *J. Comput. Phys.* **2001**, *169*, 463–502. [[CrossRef](#)]
33. Chen, S.; Merriman, B.; Osher, S.; Smereka, P. A simple level set method for solving Stefan problems. *J. Comput. Phys.* **1997**, *135*, 8–29. [[CrossRef](#)]
34. Yokoi, K.; Vaddillo, D.; Hinch, J.; Hutchings, I. Numerical studies of the influence of the dynamic contact angle on a droplet impacting on a dry surface. *Phys. Fluids* **2009**, *21*, 072102. [[CrossRef](#)]
35. Li, D.; Duan, X. Numerical analysis of droplet impact and heat transfer on an inclined wet surface. *Int. J. Heat Mass Transf.* **2019**, *128*, 459–468. [[CrossRef](#)]
36. Mino, Y.; Kagawa, Y.; Ishigami, T.; Matsuyama, H. Numerical simulation of coalescence phenomena of oil-in-water emulsions permeating through straight membrane pore. *Colloids Surf. A Physicochem. Eng. Asp.* **2016**, *491*, 70–77. [[CrossRef](#)]
37. Brackbill, J.U.; Kothe, D.B.; Zemach, C. A continuum method for modeling surface tension. *J. Comput. Phys.* **1992**, *100*, 335–354. [[CrossRef](#)]
38. Ubbink, O.; Issa, R. A method for capturing sharp fluid interfaces on arbitrary meshes. *J. Comput. Phys.* **1999**, *153*, 26–50. [[CrossRef](#)]
39. Johnson, R.E., Jr.; Dettre, R.H.; Brandreth, D.A. Dynamic contact angles and contact angle hysteresis. *J. Colloid Interface Sci.* **1977**, *62*, 205–212. [[CrossRef](#)]
40. Yeganehdoust, F.; Amer, A.; Sharifi, N.; Karimfazli, I.; Dolatabadi, A. Droplet mobility on slippery lubricant impregnated and superhydrophobic surfaces under the effect of air shear flow. *Langmuir* **2021**, *37*, 6278–6291. [[CrossRef](#)]
41. Antonini, C.; Carmona, F.; Pierce, E.; Marengo, M.; Amirfazli, A. General methodology for evaluating the adhesion force of drops and bubbles on solid surfaces. *Langmuir* **2009**, *25*, 6143–6154. [[CrossRef](#)]
42. Sakai, M.; Song, J.-H.; Yoshida, N.; Suzuki, S.; Kameshima, Y.; Nakajima, A. Direct observation of internal fluidity in a water droplet during sliding on hydrophobic surfaces. *Langmuir* **2006**, *22*, 4906–4909. [[CrossRef](#)]
43. Suzuki, S.; Nakajima, A.; Sakai, M.; Sakurada, Y.; Yoshida, N.; Hashimoto, A.; Kameshima, Y.; Okada, K. Slipping and rolling ratio of sliding acceleration for a water droplet sliding on fluoroalkylsilane coatings of different roughness. *Chem. Lett.* **2008**, *37*, 58–59. [[CrossRef](#)]
44. Wang, F.; Zhao, M. Behavior of moving droplet on inclined containment wall: Experiment and model validation. *Nucl. Eng. Des.* **2021**, *376*, 111129. [[CrossRef](#)]

**Disclaimer/Publisher’s Note:** The statements, opinions and data contained in all publications are solely those of the individual author(s) and contributor(s) and not of MDPI and/or the editor(s). MDPI and/or the editor(s) disclaim responsibility for any injury to people or property resulting from any ideas, methods, instructions or products referred to in the content.